Transportation Geotechnics 42 (2023) 101067

Contents lists available at ScienceDirect

Transportation Geotechnics

journal homepage: www.elsevier.com/locate/trgeo

Mitigation of reverse faulting in foundation soils using geosynthetic-encased granular columns

Jung Chiang [a,*], Emerson Edwige Michel [a], Kuo-Hsin Yang [a], Jorge G. Zornberg [b]

[a] Department of Civil Engineering, National Taiwan University (NTU), 1, Sec. 4, Roosevelt Rd., Taipei 106, Taiwan
[b] Department of Civil, Architectural and Environmental Engineering, The University of Texas at Austin, 301 E. Dean Keeton St., Austin, TX 78712, United States

ARTICLE INFO

Keywords:
Geosynthetic
Geosynthetic-encased granular Column (GEC)
Geosynthetic-reinforced soil (GRS) foundation
Fault
Angular distortion

ABSTRACT

In this study, a series of reduced model tests was conducted on soil foundations reinforced by Geosynthetic-Encased Granular Columns (GECs) placed across a reverse fault. These tests aimed at evaluating the effectiveness, reinforcing mechanism and optimal GEC horizontal spacing to mitigate the ground surface deformation associated with reverse faulting. For comparison, reduced model tests were also performed on unreinforced and Geosynthetic-Reinforced Soil (GRS) foundations. The reduced model tests were conducted to simulate a prototype 3-m-thick foundation layer subjected to a reverse fault displacement of 0.9 m. Digital Image Analysis (DIA) techniques were adopted to determine the surface displacement profile, angular distortion and shear rupture propagation considering various reverse fault offsets. Test results revealed that the GEC foundation can considerably reduce the fault-induced angular distortion at the ground surface. A reduction of 23.3% on the maximum angular distortion at the ground surface was observed as the fault displacement reached 30% of the foundation height (S/H = 30%), indicating the GEC foundation can mitigate the risk of surface fault hazards associated with large reverse fault movement. Two mechanisms, shear rupture diffusion and diversion effects, were identified for the GEC foundation, depending on the magnitude of the fault displacement and the system stiffness of the GEC foundation. Because of complex mechanisms between diversion and diffusion of the shear rupture in the GEC foundations, an optimal GEC spacing of $S_h/d_c = 3.3$ was observed, which exhibited the most significant reduction in β_{max} at large fault offsets.

Introduction

The surface manifestation of earthquake fault movements may result in shear rupture and differential settlements, which represent two major surface hazards for structures subjected to such fault movements [11]. Specifically, excessive shear forces and bending moments may cause severe structural damage to buildings or civil infrastructure overlying the faulting zone. In general, construction of buildings or infrastructure across or adjacent to existing fault rupture zones should be avoided. This is often codified in regulations that restrict construction of buildings within site-specific fault setbacks. However, avoiding construction across a fault zone may not be possible for linear infrastructure, such as highways, railways and roads. In such cases, geotechnical strategies should be implemented to mitigate the impact of a potential fault-induced shear rupture and associated differential settlements on the overlying infrastructure.

Studies have proposed various geotechnical strategies to mitigate problems associated with surface fault hazards [2,8,10,11,17,21,22,23,25,26,27,36,39,42]. These geotechnical strategies (summarized in Table 1) can be categorized into three groups: (1) installation of a special foundation to maintain rigid body movement of the superstructure; (2) construction of diaphragm walls or buffer trenches to divert fault ruptures; and (3) increasing the ductility of the soil materials overlying a bedrock fault to diffuse the impact of fault ruptures. Among the aforementioned strategies, increasing the ductility of soil materials, e.g., by reinforcing surface layers with geosynthetics, has typically been the most viable and cost-effective option for linear infrastructure. For example, soil layers can be reinforced with geosynthetics placed horizontally over comparatively long distances to span potential surface fault rupture zones. Studies have reported that soil ductility, often quantified as its axial strain at failure, is a controlling factor that determines the magnitude of surface deformations resulting from a surface fault rupture [9,10]. If the soil materials overlying a

* Corresponding author.
E-mail addresses: jungchiang@ntu.edu.tw (J. Chiang), d10521033@ntu.edu.tw (E.E. Michel), khyang@ntu.edu.tw (K.-H. Yang), zornberg@mail.utexas.edu (J.G. Zornberg).

https://doi.org/10.1016/j.trgeo.2023.101067
Received 17 April 2023; Received in revised form 12 July 2023; Accepted 22 July 2023
Available online 26 July 2023

Nomenclature

A_r	area replacement ratio (%)
D	maximum displacement (ft)
D_{50}	mean particle size (m)
D_r	relative density (%)
E_ϕ	efficiency factor (dimensionless)
EI	bending stiffness of GEC (kN-m^2)
G_s	specific gravity (dimensionless)
H	foundation height (m)
J_{50}	reinforcement tensile stiffness (kN/m)
L	total length of foundation (m)
L_I	fault influence length (m)
L_R	reinforcement length (m)
M_L	Richter magnitude (dimensionless)
R_d	percentage reduction for maximum angular distortion (%)
S	fault offset/vertical fault displacement (m)
S_h	horizontal spacing of GEC (m)
S_v	reinforcement vertical spacing (m)
T	reinforcement tensile force (kN/m)
T_{ult}	reinforcement ultimate tensile strength (kN/m)
c'	effective cohesion (kPa)
d_c	diameter of GEC (m)
l_c	embedded length of GEC (m)
l_{ij}	horizontal distance between reference points i and j (m)
n	number of reinforcement layers (dimensionless)
x	distance to the left boundary (m)
α	dip angle of normal fault (°)
β_{allow}	allowable angular distortion
β_{ij}	angular distortion between reference points i and j (dimensionless)
β_{max}	maximum angular distortion (dimensionless)
$\beta_{max,\ r}$	maximum angular distortion of reinforced foundation (dimensionless)
$\beta_{max,\ u}$	maximum angular distortion of unreinforced foundation (dimensionless)
γ_d	dry unit weight (kN/m^3)
$\gamma_{d,\ \max}$	maximum dry unit weight (kN/m^3)
$\gamma_{d,\ \min}$	minimum dry unit weight (kN/m^3)
γ_{xy}	soil shear strain (dimensionless)
λ	target scaling ratio (dimensionless)
δ	surface settlement (m)
δ'	effective interface friction angle (degree)
δ_{ij}	vertical displacement between reference points i and j (m)
ε	reinforcement tensile strain (%)
ε_a	soil axial strain (%)
ε_f	reinforcement tensile strain at failure (%)
ε_v	soil volumetric strain (%)
ε_{ult}	reinforcement ultimate tensile strain (%)
σ_3	confining pressure (kPa)
σ_d	deviatoric stress (kPa)
σ_n	normal stress on the soil-reinforcement interface (kPa)
σ_v	overburden pressure (kPa)
ϕ'	effective peak friction angle (degree)

Table 1
Summary of geotechnical strategies for surface fault hazards proposed in past studies.

References	[a] Fault type	Mitigations
Bray et al. (1993)	*N/R*	Geosynthetic-reinforced compacted fills
Bray (2001)	*N/R*	Avoidance/geotechnical approach (reinforced earth fills)
Gazetas et al. (2008)	*N/R*	Continuous and rigid foundation systems (mat or box type)
Faccioli et al. (2008)	*N*	Rigid, continuous and flexible foundation systems
Bray (2009)	*N/R*	Ductile earth fills/soil reinforcement/slip layers/strong and ductile foundations (thickened reinforced mat foundation, waffle slabs and post-tensioned slabs), etc.
Oettle and Bray (2013)	*N/R*	Diffusion of fault rupture (ductile engineered fill)/rigid-body movement (thick mat foundation, decoupling of foundation and soil)/diversion of fault rupture (ground improvement, diaphragm wall, basement, ground anchors, seismic gap)
Fadaee et al. (2016)	*R*	Soil-bentonite wall
Ashtiani et al. (2017)	*R*	Vertical trench adjacent to foundation/reinforced zone beneath foundation
Loli et al. (2018)	*R*	Hybrid foundations (integrated with footings and cofferdam or skirts)
Garcia and Bray (2019a, b)	*N/R*	Rigid and continuous foundations
Yang et al. (2020)	*N*	Geosynthetic-reinforced soil foundations
Chiang et al. (2021)	*N*	Geosynthetic-reinforced soil foundations
Firouzeh et al. (2022)	*R*	Wall barriers (Expanded Polystyrene [EPS] geofoam, soil-bentonite and Lightweight Expanded Clay Aggregate [LECA])

[a] N = normal fault; R = reverse fault.

bedrock fault are brittle, the fault rupture will be reflected through the overlying soil layer and reach the ground surface, resulting in failure of the superstructures. However, if the overlying soil layer is ductile (or relatively thick), the fault rupture displacements will be dissipated over a relatively wide influence zone, thereby producing relatively smooth ground deformation.

Geosynthetic-Reinforced Soil (GRS) structures have been implemented in engineering practice to mitigate surface faulting hazards. In Central Taiwan, for example, a highway embankment was constructed across the Chelungpu Fault. In the 1999 Chi-Chi earthquake ($M_L = 7.3$), the vertical surface movement ranged from 5 to 7 m along the major thrust of the Chelungpu Fault, which resulted in failure of much of the overlying buildings and infrastructure [16]. This included the failure of rigid gravity retaining walls, which were attributed to the considerable surface rupturing induced by the fault movement. To reduce the reoccurrence of similar events, the Chelungpu Fault was subsequently traversed by constructing a ductile highway embankment comprising a GRS wall overlying a GRS foundation. Fig. 1 presents an aerial view of the embankment. Yang et al. [42] conducted a series of reduced model tests to investigate the performance of GRS foundations subjected to normal fault movement. The test results revealed that GRS foundations can reduce fault-induced angular distortions at the ground surface by up to 60% in comparison with unreinforced foundations. This reduction could be attributed to the development of reinforcement tensioned membrane and shear rupture interception effects. Chiang et al. [17] conducted numerical simulations aimed at developing design methods for GRS foundations on the mitigation of ground deformation induced by normal fault movement. Although studies have validated the benefits

Fig. 1. Aerial view of the GRS embankment constructed in Taiwan to mitigate hazards posed by a potential surface fault rupture.

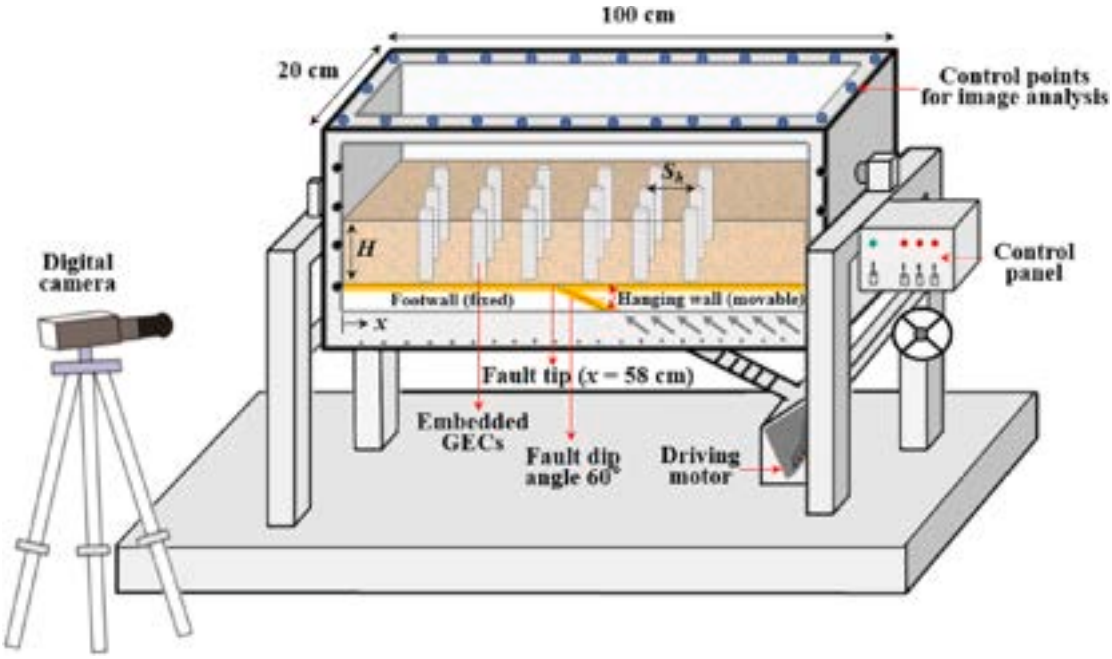

Fig. 2. Illustration of sandbox and reduced-scale model test setup.

of using GRS foundations to mitigate normal fault hazards, the performance of GRS foundations subjected to reverse fault movement is not yet understood. In fact, GRS foundations may not effectively reduce reverse fault-induced ground deformation. Sufficient mobilized tensile force was not developed within the reinforcements because the reinforcement was subjected to compression as reverse fault displacement occurred (i.e., the hanging wall moves upward). Accordingly, another type of reinforced soil foundation, Geosynthetic-Encased Granular Columns (GECs), was proposed and investigated in this study to overcome such deficiencies and provide informative design implications of using GEC foundations in reverse fault hazard mitigation. The investigated GEC foundation is intended to support a GRS wall as a highway embankment to reduce the extent of fault-induced angular distortion to an acceptable level and maintain the stability of the overlying GRS wall. The performance of GEC foundations (i.e., the effectiveness and reinforcing mechanisms of GEC foundations, and the optimal horizontal spacing of GECs) subjected to reverse fault movement was evaluated.

GECs have commonly been used to support road embankments that overlie extremely weak soils as they provide not only vertical support to road embankments but also enhance clay subsoils by accelerating its consolidation. Experimental and numerical studies have investigated the effectiveness of GECs in improving the bearing capacity of extremely weak soils and evaluated the failure mechanisms of GECs under vertical loading conditions, such as bulging and punching [1,6,14,15,18,19,28,29,31,33,34,40]. Researchers have also evaluated the mechanical behavior of GECs embedded in weak soils and subjected to lateral loading conditions [13,30,37,38,45]. The shear and bending resistance of GECs against lateral loads or displacement are key factors that may significantly influence the performance of GEC foundations in surface fault hazard mitigation. These studies have indicated that geotextile encasement can considerably improve the overall performance of sand or stone columns subjected to lateral loads or displacement. However, most of these studies focused only on the mechanical behavior of GECs embedded in weak cohesive soils in road embankments. However, the performance of GEC-reinforced granular soil foundations subjected to fault movement has not been evaluated in previous studies

Table 2
Experimental program and results of unreinforced and GRS foundation tests at maximum fault offset.

Test	Test ID	Test variables				Test results [a]	
		Number of reinforcement layers n	Horizontal spacing of GEC S_v (cm)	Foundation height H (cm)	Reinforcement stiffness J_{50} (kN/m)	Maximum angular distortion β_{max}	Percentage reduction [b] R_d (%)
Unreinforced foundation	U	–	6.67	20	–	0.84	–
GRS foundation	R-3L	3	6.67	20	5.5	0.84	0

[a] test results at $S = 6$ cm.
[b] compared to the β_{max} of the unreinforced foundation (Test U).

Table 3
Experimental program and results of GEC foundation tests at maximum fault offset.

Test	Test ID	Test variables					Test results [a]		
		Diameter of GEC d_c (cm)	Horizontal spacing of GEC S_h (cm)	Foundation height H (cm)	Reinforcement stiffness J_{50} (kN/m)	Area replacement ratio A_r (%)	Maximum angular distortion β_{max}	Percentage reduction [b] R_d (%)	Major reinforcing mechanism
GEC foundation	GEC8	3	8	20	5.5	11.03	0.71	15	Diversion
	GEC10 (baseline)	3	10	20	5.5	7.06	0.64	23.3	Diversion and diffusion
	GEC14	3	14	20	5.5	3.6	0.67	20	Diffusion

[a] test results at $S = 6$ cm.
[b] compared to the β_{max} of the unreinforced foundation (Test U).

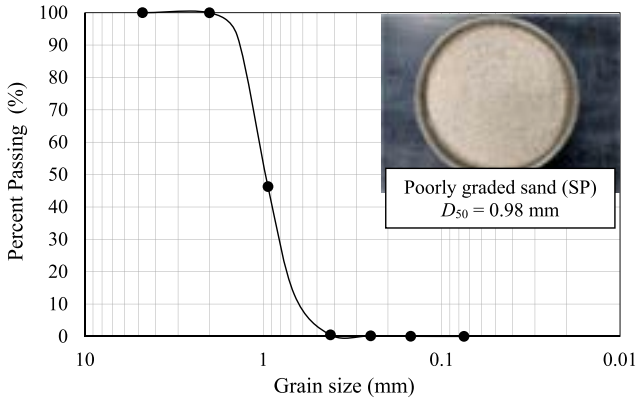

Fig. 3. Grain size distribution curve and photo of test sand.

and is not fully understood.

To address this gap in the state of knowledge, reduced model tests were conducted to investigate the performance of GEC foundations in mitigating the surface hazards associated with reverse faulting. For comparison, reduced model tests were also performed on unreinforced and GRS foundations. The reduced model tests were conducted to simulate a prototype 3-m-thick foundation layer subjected to a reverse fault displacement of 0.9 m. Digital Image Analysis (DIA) techniques were adopted to determine the surface displacement profile, angular distortion and shear rupture propagation at various reverse fault offsets. The effectiveness of a GEC foundation and reinforcing mechanisms of geotextile encasement to mitigate ground surface deformation were investigated.

Reduced model tests

Model characteristics and scope of the testing program

The reduced-scale models tested in this investigation included unreinforced, GRS and GEC foundations. The reduced model tests were conducted using a sandbox in the geotechnical research laboratory at National Taiwan University. Fig. 2 presents an illustration of the sandbox and overall test setup. The sandbox dimensions are 100 cm × 20 cm × 60 cm (length × width × height). From the surface displacement profiles and shear strain contours obtained in the reduced model tests, it can be noticed that the surface displacement at the left and right boundaries was zero and the fault-induced shear rupture did not reach the boundaries of the sandbox, indicating that the boundary condition has a minor effect on the ground surface deformation and shear rupture development. The front and back walls of the sandbox consist of transparent plexiglass for visual observation during testing. The plexiglass walls were lined using lubricated thin plastic sheets to minimize soil–wall interface friction. The bottom of the sandbox comprises a movable

Table 4
Soil and reinforcement properties.

Properties	Value
Soil	
Soil classification (USCS)	SP
Specific gravity, G_s	2.65
Mean grain size, D_{50} (mm)	0.98
Min. dry unit weight, $\gamma_{d,\ min}$ (kN/m^3)	13.5
Max. dry unit weight, $\gamma_{d,\ max}$ (kN/m^3)	16.4
Relative density, D_r (%)	70
Target dry unit weight, γ_d (kN/m^3)	15.3
Cohesion, c' (kPa)	0
Peak friction angle, ϕ' (°)	39.2
Reinforcement	
Type	Nonwoven geotextile
Material	Polypropylene (PP)
Mass per unit area (g/m^2)	29.6
Thickness (mm)	0.235
Ultimate tensile strength, T_{ult} (kN/m)	[a] 0.7/0.29
Ultimate tensile strain, ε_{ult} (%)	[a] 32.4/87.4
Tensile stiffness, J_{50} (kN/m)	[a] 5.47/0.46
Soil-reinforcement interface	
Peak interface friction angle, δ'	27.4
Efficiency factor, E_ϕ	0.63

[a] values before and after slash are tensile strength properties tested in machine and cross-machine directions, respectively.

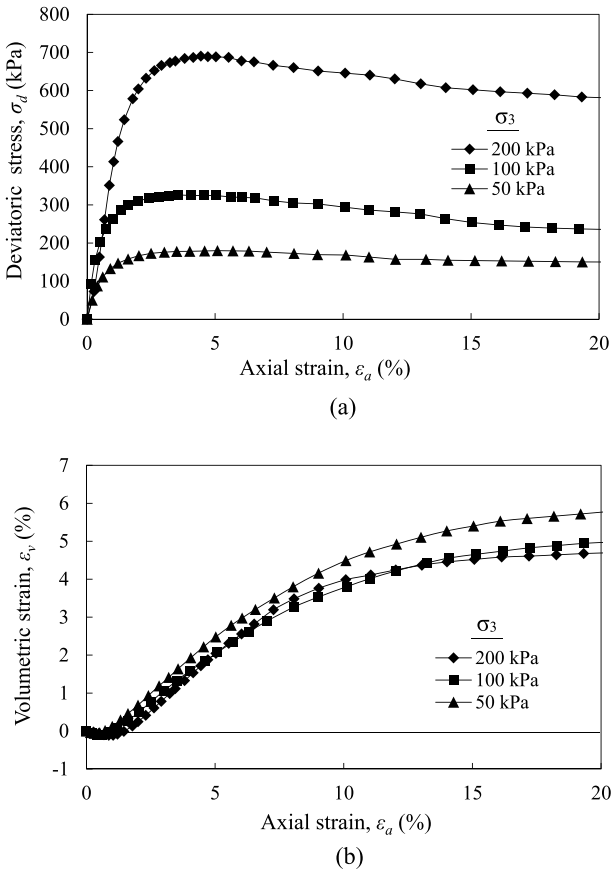

Fig. 4. Triaxial consolidated-drained test results of test sand: (a) deviatoric stress vs. axial strain; and (b) volumetric strain vs. axial strain.

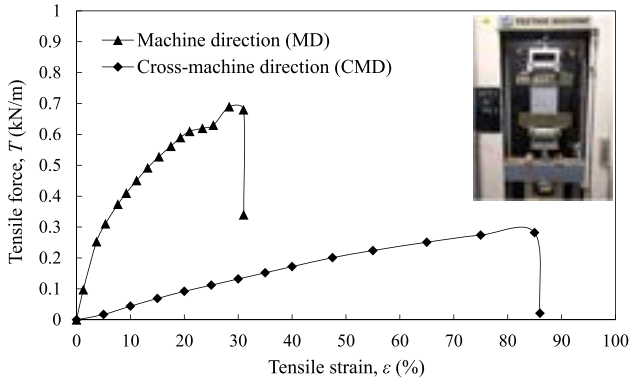

Fig. 5. Wide-width tensile test results for nonwoven geotextile.

hanging wall and a fixed footwall. Reverse fault displacement was generated by moving the hanging wall upward using a driving motor installed under the sandbox. The initial location of the reverse fault tip was $x = 58$ cm from the left boundary and the fault dip angle was set to 60°.

Tables 2 and 3 summarize the scope of the experimental test program conducted in this study as well as the corresponding variables for the reduced model tests. A total of five model tests were conducted. Tests U and R-3L in Table 2 denote the tests conducted on the unreinforced and GRS foundations, respectively, which were carried out to compare the performance of GEC foundations. The remaining three tests in Table 3 were GEC foundation tests and numbered as follows: GEC denotes a GEC foundation and the subsequent number denotes the GEC horizontal

Table 5
Scaling factors and values based on similitude requirements.

Parameters	[a] Scaling factor	Model	Prototype
Geometry			
Foundation height, H (m)	$1/\lambda$	0.2	3.0
Soil parameter			
Target dry unit weight, γ_d (kN/m^3)	1	15.3	15.3
Friction angle, ϕ' (°)	1	39.2	39.2
Reinforcement parameter			
Ultimate tensile strength, T_{ult} (kN/m)	$1/\lambda^2$	[b] 0.7	157.5
Tensile stiffness, J_{50} (kN/m)	$1/\lambda^2$	[b] 5.47	1231
Interface parameter			
Soil-geosynthetic friction angle, δ'	1	27.4	27.4
GEC parameter			
Bending stiffness, EI (kN-m^2)	$1/\lambda^5$	6.35×10^{-4}	482.2

[a] target scaling ratio $\lambda = 15$.
[b] tensile strength properties tested in machine direction.

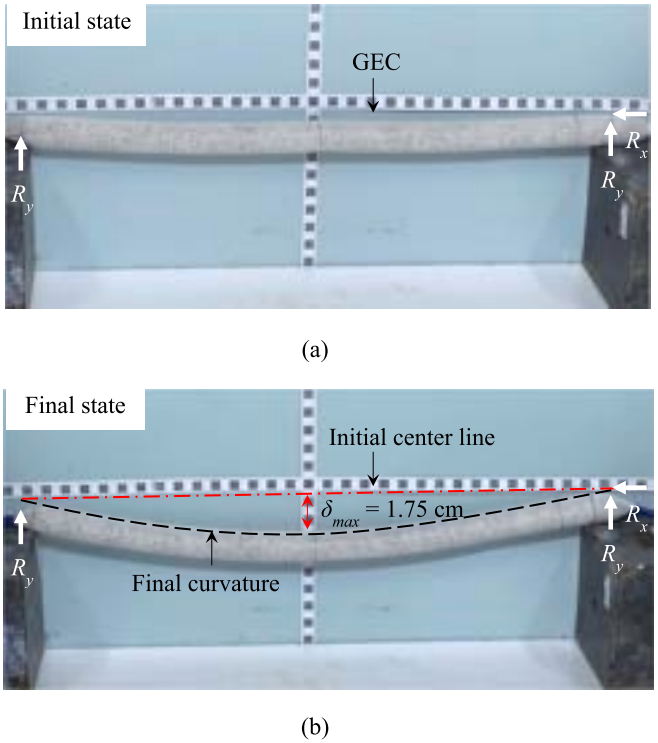

Fig. 6. Illustration of bending stiffness tests on GECs: (a) initial state; and (b) deflection at final state.

spacing in centimeters. For example, Test GEC10 corresponds to the test conducted on a GEC foundation with a horizontal spacing of 10 cm. GEC10 was used as the baseline case for a parametric study evaluating the influence of GEC spacing on the performance of GEC foundations.

Material properties

The soil material used in the reduced model tests was uniform quartz sand, which classifies as poorly graded sand (SP) according to the Unified Soil Classification System (USCS). Fig. 3 displays the grain size distribution curve and a photograph of the sand used in this study. The material properties of the test sand were determined in accordance with the American Society for Testing and Materials (ASTM) standards (Table 4). The mean particle size of the sand was $D_{50} = 0.98$ mm, and the target dry unit weight was $\gamma_d = 15.3$ kN/m^3 at a relative density $D_r = 70\%$. The effective cohesion and peak friction angle of the test sand were

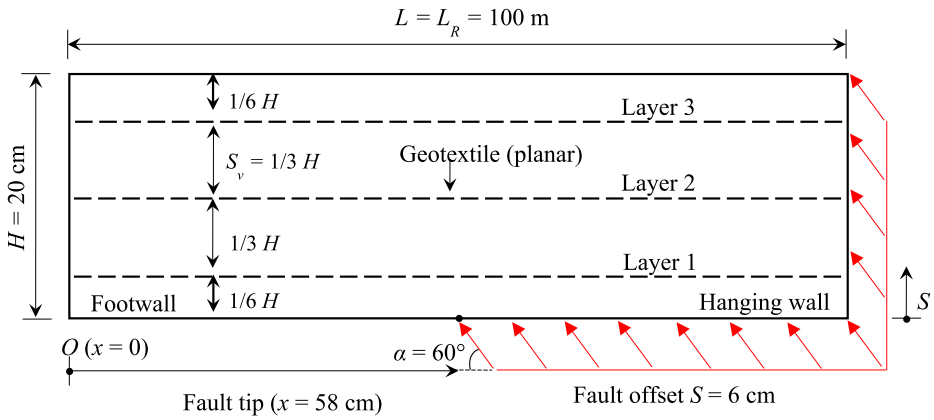

(a)

(b)

Fig. 7. GRS foundation test (Test R-3L): (a) illustration (not to scale); and (b) photo of test.

$c' = 0$ kN/m^2 and $\phi' = 39.2°$, respectively; these values were obtained from triaxial consolidated–drained (CD) compression tests [5]. Fig. 4 depicts the stress–strain–volumetric strain curves for the sand used in this study also obtained from the triaxial CD tests. The test sand exhibited strain softening behavior at high confining pressure. The strain at failure of the test sand ranged from 2% to 5% for confining pressures ranging from $\sigma_3 = 50$ to 200 kPa, which indicated the test sand was relatively brittle at the target relative density.

The reinforcement material used in the reduced model tests was a nonwoven polypropylene geotextile, the material properties of which are listed in Table 4. Wide-width tensile tests [3] in the machine and cross-machine directions were conducted to evaluate the tensile strength properties of the reinforcement, and the results are presented in Fig. 5. In the machine direction, the ultimate tensile strength and failure strain of the nonwoven geotextile were $T_{ult} = 0.7$ kN/m and $\varepsilon_f = 32.4\%$, respectively, and the tensile stiffness at a stress level of 50% of the ultimate tensile strength was $J_{50} = 5.47$ kN/m. In the cross-machine direction, the ultimate tensile strength and failure strain were $T_{ult} = 0.29$ kN/m and $\varepsilon_f = 87.4\%$, respectively, and the tensile stiffness at 50% of the ultimate tensile strength was $J_{50} = 0.46$ kN/m. The longitudinal direction of the reinforcement material used in the GRS foundation test (indicated herein as planar geotextile) was oriented parallel to the designated machine direction to achieve high mobilized tensile force against reverse fault movement (i.e., the strong direction of the planar geotextile was oriented perpendicular to the reverse fault rupture). For the geotextile encasement used in the GEC foundation tests, the nonwoven geotextile was oriented in the designated machine direction in the circumferential direction of the geotextile encasement to develop hoop stress. Additionally, to account for interactions between the nonwoven geotextile and adjacent sand, interface direct shear tests [4] were conducted. The sand–geotextile interface friction angle obtained was $\delta' = 27.4°$ and the efficiency factor was calculated to be $E_\phi = \tan\delta'/\tan\phi' = 0.63$.

To establish that the 1g test models and prototypes exhibited comparable behavior, similitude analyses were conducted to identify the relationship between the physical quantities of the 1g test models and those of prototypes. The material properties adopted in the 1g reduced model tests were scaled down using scaling factors derived in accordance with Buckingham π Theorem [12]. Table 5 summarizes the scaling factors and corresponding values in prototype for the model geometry and material properties. These scaling factors have been adopted in numerous studies on 1g reduced model tests of GRS walls [24,41,43,44] to consider the similarity of 1g test models. A geotextile with a comparatively low tensile strength was selected to fulfill similitude requirements for the reduced model tests. Based on these requirements, the tensile strength properties of the reinforcement should be scaled down to $1/\lambda^2$ of the prototype tensile properties, where λ is the target scaling ratio. In accordance with the design height of the foundations and dimensions of the sandbox, a target scaling ratio of $\lambda = 15$ was selected for this study. Therefore, the tensile properties of the model reinforcement were scaled down 225 times to fulfill similitude requirements.

In addition to the aforementioned material properties, the bending stiffness of a GEC, which is usually expressed as *EI*, is a key property influencing the performance of a GEC foundation. Fig. 6 displays photographs of bending stiffness tests conducted in this study. The GEC

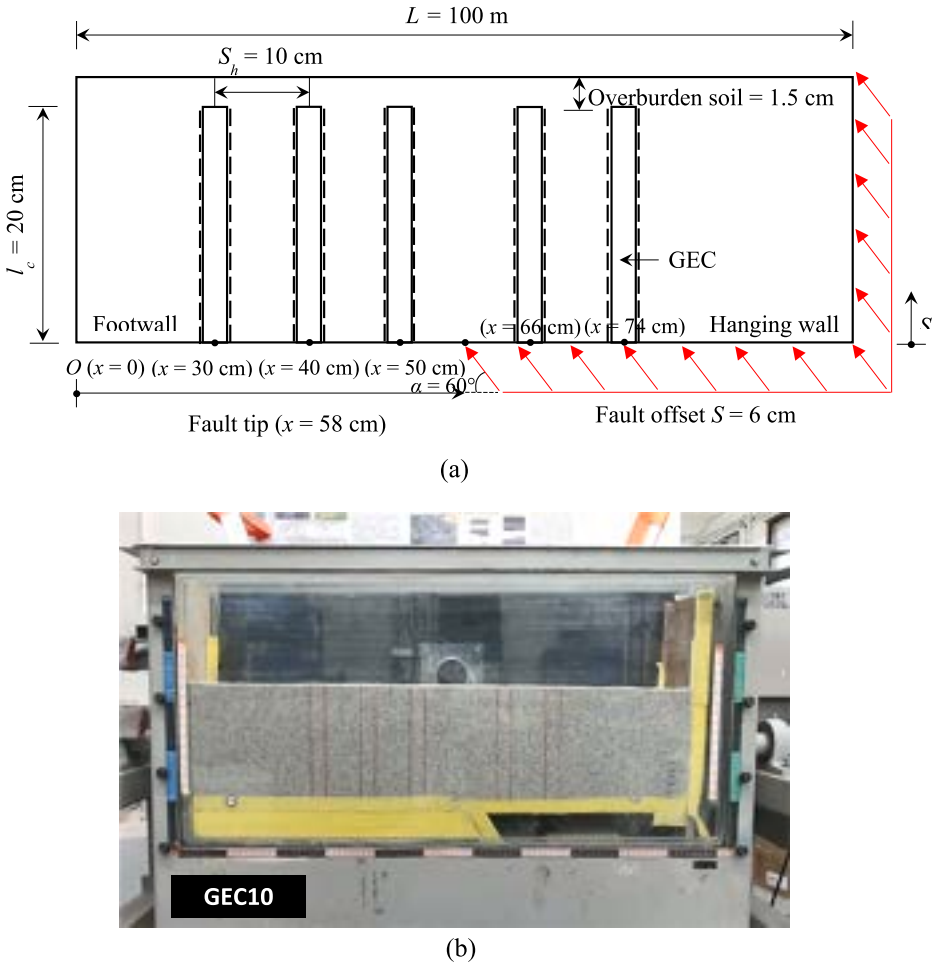

Fig. 8. Baseline GEC foundation test (Test GEC10): (a) illustration (not to scale); and (b) photo of test.

specimen used for the bending stiffness tests had a diameter of $d_c = 3$ cm, length of $l_c = 53$ cm and was prepared at a target relative density of $D_r = 70\%$ with soil and reinforcement materials identical to those used in the reduced model tests. The GEC specimen was supported horizontally at the edges by two iron blocks and the deflection that developed in the middle due to self-weight was measured. The bending stiffness of the GEC was then back-calculated using the deflection equation for a linear continuous beam. The test results revealed that the bending stiffness of the GEC was $EI = 6.35 \times 10^{-4}$ kN-m^2, corresponding to a value of 482.2 kN-m^2 in prototype (a scaling factor of $1/\lambda^5$, as derived using Buckingham π Theorem). The bending stiffness of the GEC was significantly lower than a conventional concrete pile, indicating that the GEC foundation can be considered as a flexible reinforced system. However, it should be noticed that the bending stiffness of the GEC was measured under self-weight and simply support conditions. The bending stiffness of the GEC may vary as it was embedded in the foundation soil. Different loading conditions could cause different EI values and thus deformation behavior of the GECs. The scaling factor and corresponding value for the bending stiffness of the GEC in prototype are presented in Table 5.

Model preparation and test procedure

For the GRS foundation test, placement of a soil layer followed by a planar geotextile layer was repeated until the desired foundation height was reached (i.e., the height of the reduced-scale GRS foundation model was $H = 20$ cm). The soil layer was constructed with a target relative density $D_r = 70\%$ using the volume control method. The weight of sand required for the soil layer was calculated and pluviated from a hopper into the sandbox at a constant falling height and moving rate, after which the soil layer was carefully compacted to achieve uniform target relative density. Past studies [17,42] have investigated the influences of reinforcement spacing and number on the performance of GRS foundations subjected to surface fault movement. These studies suggested that a 3-layer GRS foundation with a uniform vertical spacing (i.e., $S_v = 1/3H$) had an optimal effect in minimizing the fault-induced angular distortion at the ground surface. Therefore, three layers of planar geotextile were placed in the GRS foundation with a uniform vertical spacing of $S_v = 6.67$ cm. The two ends of the planar geotextile were clamped on rigid steel rods which were firmly fixed on the left and right boundaries of the sandbox. This approach was designed to simulate the field condition in which the length of the reinforcement is long enough such that reinforcement pullout does not occur within the fault influence zone. Plastic markers were attached to the longitudinal edges of the planar geotextile at specific horizontal spacings to monitor the deformation of the embedded reinforcement. Fig. 7 provides a schematic and a picture of the GRS foundation model before testing. According to the reduced model test similitude laws, the foundation was equivalent to a height of 3 m in prototype for the target scaling ratio of $\lambda = 15$ selected for this study.

In the GEC foundation tests, low-friction stainless steel tubes were used to construct the GECs. Lubricated steel tubes were inserted into a full-height soil layer (i.e., the height of the reduced-scale GEC foundation model was $H = 20$ cm) at the desired locations. The location of the outermost GEC installed in the footwall was determined by considering the influential zone of the free-field fault rupture. Each steel tube had a thin-walled tip to minimize disturbance to the soil layer. The geotextile

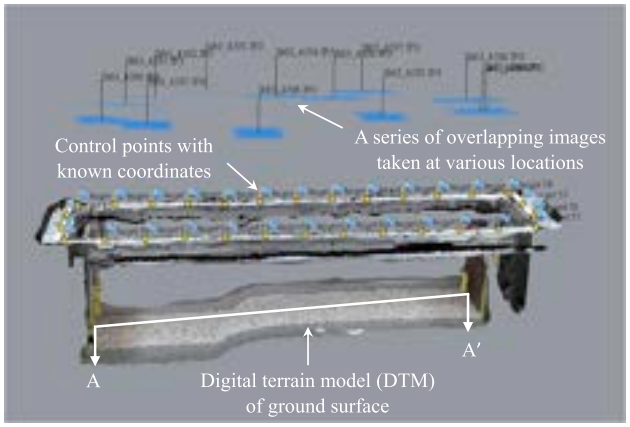

(a)

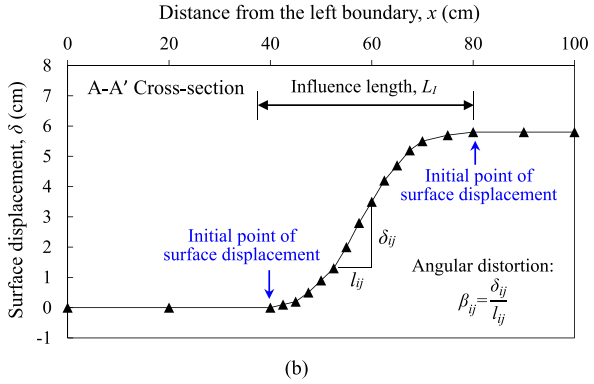

(b)

Fig. 9. Determination of ground surface deformation: (a) Digital Terrain Model (DTM); and (b) surface displacement profile (A-A' cross-section).

encasements were fabricated in advance, placed into the steel tubes, filled with the soil material and compacted to the target relative density. After the installation was completed, the steel tubes were carefully removed from the soil layer. A 1.5-cm-thick soil layer was then constructed on top of the GEC foundations to provide overburden pressure. Fig. 8 displays a schematic and a picture of the baseline GEC foundation test (Test GEC10). The diameter of the GECs was $d_c = 3$ cm, corresponding to a diameter of 0.45 m in prototype scale, and the length-to-diameter ratio of the GECs was $l_c/d_c = 0.67$. A fault displacement was induced after construction of the test models with a maximum fault displacement set at $S = 6$ cm due to the limited displacement capacity of the sandbox. The ratio of fault displacement to foundation height was $S/H = 30\%$. According to the similitude laws, the reduced-scale model tests simulated a reverse fault displacement up to 90 cm in prototype.

During the reduced model tests, charge-coupled device cameras, aimed at the front and top of the sandbox, were used for continuous monitoring of test model deformation. The photographic data captured were analyzed using various DIA techniques to obtain the surface displacement profile, maximum angular distortion, and shear rupture propagation for the unreinforced, GRS, and GEC foundations at various fault offset magnitudes. The surface displacement profiles were obtained from Digital Terrain Models (DTMs) established using digital images of the top of the test models. Because the ground surface deformation induced by fault movement critically affects superstructure damage, the maximum angular distortion at the ground surface (β_{max}) was used in this study as a key indicator to evaluate the performance of the unreinforced, GRS and GEC foundations. The angular distortion at the ground surface was determined from the surface displacement profile as follows:

$$\beta_{ij} = \frac{\delta_{ij}}{l_{ij}} \tag{1}$$

where β_{ij} is the angular distortion (i.e., the tangent of distortion angle); δ_{ij} and l_{ij} are the vertical displacement and horizontal distance between reference points i and j, respectively. The β_{max} was simply determined as the maximum value of β_{ij} (i.e., the steepest slope) along the surface displacement profile. To quantify the performance of the GRS and GEC foundations in reducing β_{max} at the ground surface, a percentage reduction for β_{max} (expressed as R_d) was adopted. The parameter R_d is expressed as follows:

$$R_d(\%) = \frac{\beta_{max,u} - \beta_{max,r}}{\beta_{max,u}} \times 100\% \tag{2}$$

where $\beta_{max,\ u}$ and $\beta_{max,\ r}$ are the maximum angular distortions of the unreinforced and reinforced (GRS or GEC) foundations, respectively. The horizontal distance between two initial points of the surface

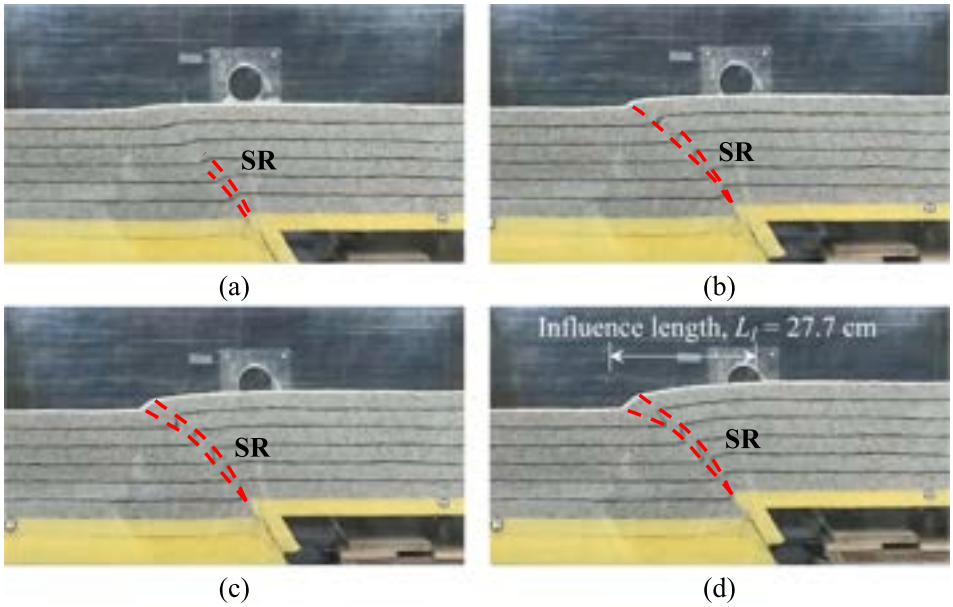

Fig. 10. Photos of unreinforced foundation test (Test U) at various fault offsets: (a) $S = 1.5$ cm; (b) $S = 3$ cm; (c) $S = 4.5$ cm; and (d) $S = 6$ cm.

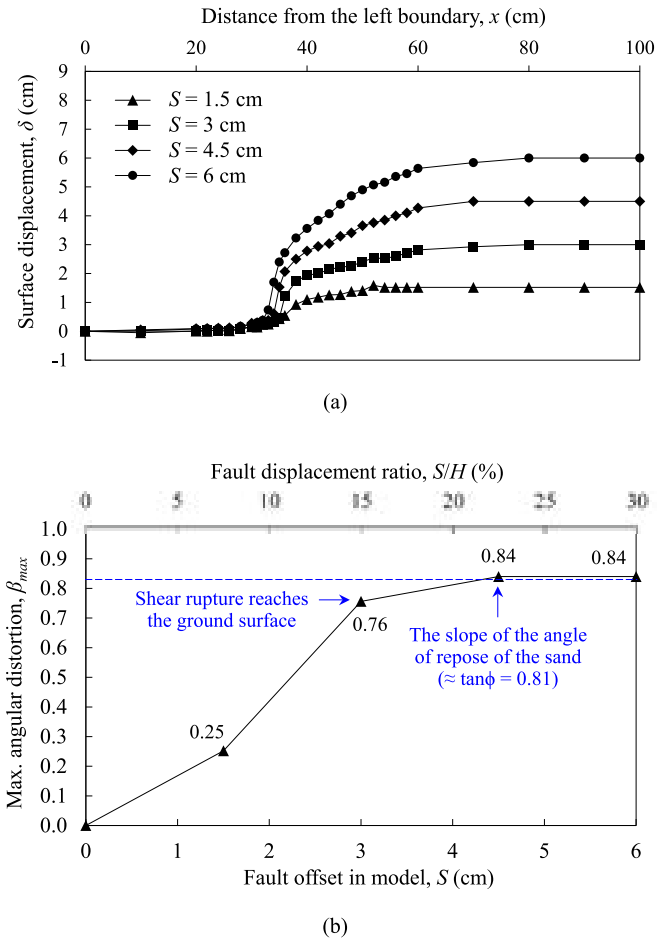

Fig. 11. Ground deformation of unreinforced foundation test (Test U) at various fault offsets: (a) surface displacement profile; and (b) maximum angular distortion.

displacement (defined as the fault influence length L_I) was evaluated to analyze the reinforcing mechanisms of the GRS and GEC foundations under reverse faulting. An illustration of the DTM for the determination of surface displacement profiles, and definitions of maximum angular distortion and fault influence length are presented in Fig. 9.

In addition to ground surface deformation, the shear rupture propagation of the unreinforced, GRS, and GEC foundations was also analyzed to evaluate the reinforcing mechanisms of the GRS and GEC foundations under reverse faulting. The shear strain contours at various fault offsets, which were established using Digital Image Correlation (DIC) techniques, were selected to represent the shear rupture propagation that developed within the test models. To facilitate DIC, successive high-resolution photos of the front of the test models were captured during testing. Black sand was mixed into the soil material for tracing soil particle movement. Details of the DIC techniques used in this study are provided in Yang et al. [42].

Results and discussion

Unreinforced foundation

Fig. 10 presents a series of images from the unreinforced foundation test involving reverse fault movement at fault offsets of $S = 1.5$, 3, 4.5 and 6 cm. The test results indicate that the ground surface deformation became pronounced as the reverse fault displacement increased (Figs. 10 and 11a). The β_{max} at the ground surface were 0.25, 0.76, 0.84, and 0.84 at $S = 1.5$, 3, 4.5, and 6 cm, respectively (Fig. 11b). As expected, the β_{max} at the ground surface increased as the fault displacement increased and approached the slope of the sand's angle of repose ($\approx \tan\phi = 0.81$) at large fault offsets. The fault influence length was $L_I =$ 27.7 cm at $S = 6$ cm.

Fig. 12 shows the shear strain contours of the unreinforced foundation subjected to reverse fault movement. The shear rupture propagated upward from the fault tip to the ground surface and decreased in dip as it approached the ground surface. At $S = 3$ cm ($S/H = 15\%$), the shear rupture broke through the foundation soil and a surface fault rupture occurred at the ground surface. Meanwhile, the β_{max} at the ground surface increased considerably, from 0.25 to 0.76 (Fig. 11b), indicating a high surface fault hazard risk. The aforementioned results are in good agreement with those of the centrifuge tests conducted by Lin et al. [35] and field observations presented by Bray et al. [9].

GRS foundation

Fig. 13 displays a series of images from the GRS foundation tests involving reverse fault movement at fault offsets of $S = 1.5$, 3, 4.5 and 6 cm. When reverse fault displacement occurred, the ground surface deformed in a manner similar to that of the unreinforced foundation

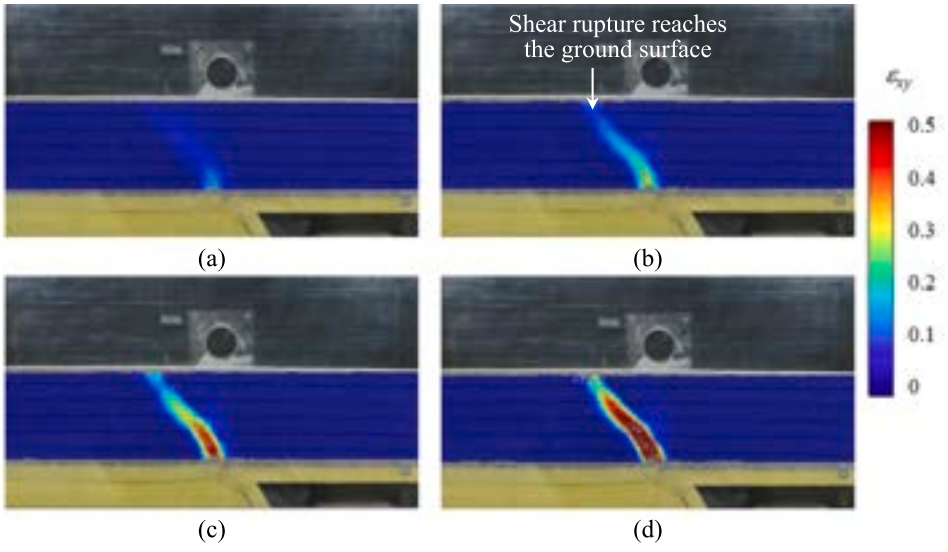

Fig. 12. Shear rupture propagation of unreinforced foundation test (Test U) at various fault offsets: (a) $S = 1.5$ cm; (b) $S = 3$ cm; (c) $S = 4.5$ cm; and (d) $S = 6$ cm.

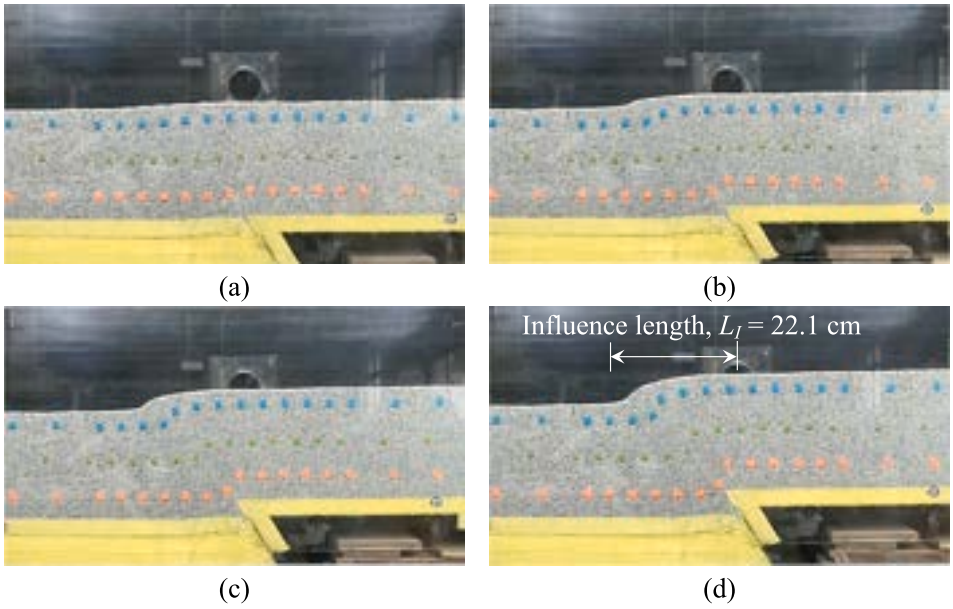

Fig. 13. Photos of GRS foundation test (Test R-3L) at various fault offsets: (a) S = 1.5 cm; (b) S = 3 cm; (c) S = 4.5 cm; and (d) S = 6 cm.

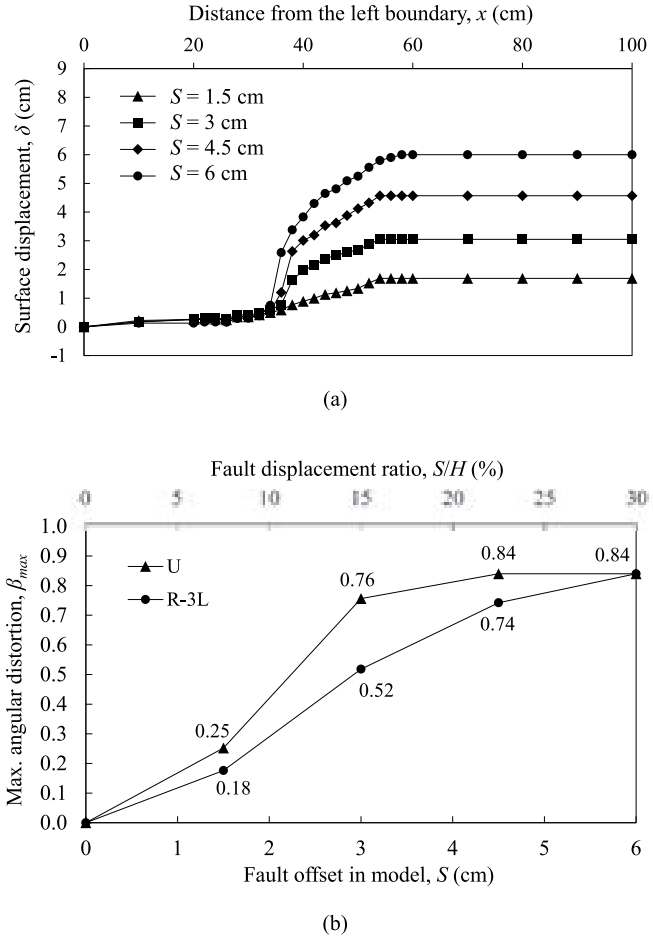

Fig. 14. Ground deformation of GRS foundation test (Test R-3L) at various fault offsets: (a) surface displacement profile; and (b) maximum angular distortion.

(Figs. 11a and 14a). The fault influence length was L_I = 22.1 cm at S = 6 cm, which is similar to the fault influence length of the unreinforced foundation (i.e., L_I = 27.7 cm). The β_{max} values were 0.18, 0.52, 0.74, and 0.84 at S = 1.5, 3, 4.5, and 6 cm, respectively (Fig. 14b). The percentage reduction for β_{max} at S = 1.5, 3, 4.5, and 6 cm was R_d = 30.2%, 31.5%, 11.7%, and 0%, respectively. The test results revealed that the GRS foundation was effective in reducing β_{max} at small fault offsets of S = 1.5 and 3 cm (i.e., a fault displacement ratio of S/H < 15%). However, the effectiveness in reducing β_{max} decreased considerably after the shear rupture reached the ground surface (i.e., at S = 4.5 cm, as shown in Fig. 15). The percentage reduction for β_{max} decreased to zero (R_d = 0%) at large fault offset of S = 6 cm (S/H = 30%). In the reduced model test of GRS foundations subjected to normal fault movement conducted by Yang et al. [42], the reduction in β_{max} induced by normal faulting was attributed to the development of the tensioned membrane and shear rupture interception effects. However, these effects were not observed for the GRS foundation subjected to reverse fault movement. Similar shear strain contours were obtained for the unreinforced and GRS foundations (Figs. 12 and 15, respectively) because the mobilization of the reinforcement tensile force had not sufficiently developed when the hanging wall was moving upward (i.e., the GRS foundation was compressed). Nonetheless, despite the considerable increase in β_{max} at large fault offsets, β_{max} was notably reduced at small fault offsets because of increased foundation ductility (i.e., axial strain at failure) caused by soil–geosynthetic interaction.

In summary, the GRS foundation notably reduced the β_{max} at the ground surface at small fault offsets. However, the GRS foundation became ineffective in reducing β_{max} at large fault offsets. The R_d value decreased to 0% at S/H = 30% due to insufficient mobilized tensile force within the reinforcement because the GRS foundation was mainly subjected to compression as reverse fault displaced.

GEC foundation

Fig. 16 presents a series of images from the GEC foundation tests involving reverse fault movement (Test GEC10, the baseline case) at various fault offsets. Stepped surface displacement profiles were observed as the reverse fault displacement increased (Fig. 17a). The β_{max} were 0.17, 0.34, 0.59, and 0.64 at S = 1.5, 3, 4.5, and 6 cm, respectively (Fig. 17b). Compared with the unreinforced foundation, the β_{max} at the ground surface significantly decreased. The percentage reductions for β_{max} at S = 1.5, 3, 4.5, and 6 cm were R_d = 33.3%, 55.6%, 30%, and 23.3%, respectively. The fault influence length was L_I = 38.6 cm at S = 6

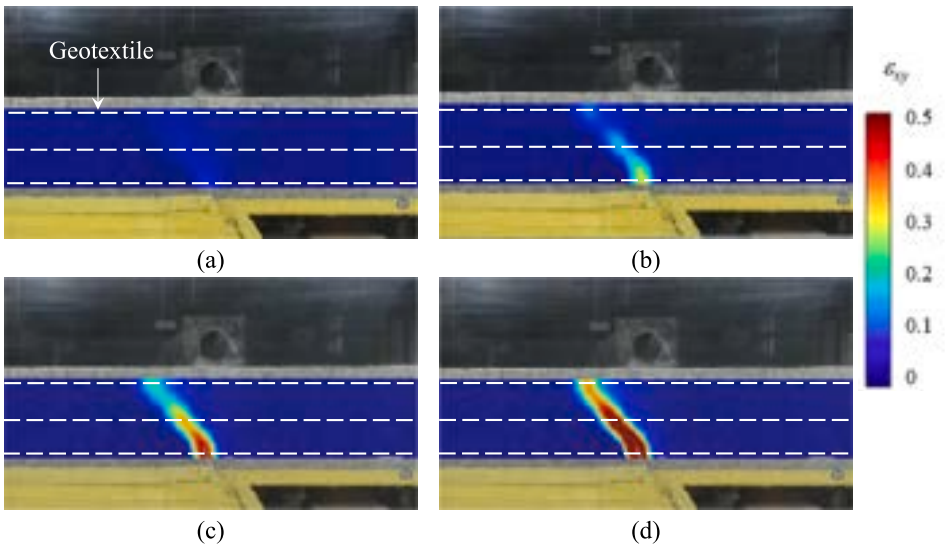

Fig. 15. Shear rupture propagation of GRS foundation test (Test R-3L) at various fault offsets: (a) $S = 1.5$ cm; (b) $S = 3$ cm; (c) $S = 4.5$ cm; and (d) $S = 6$ cm.

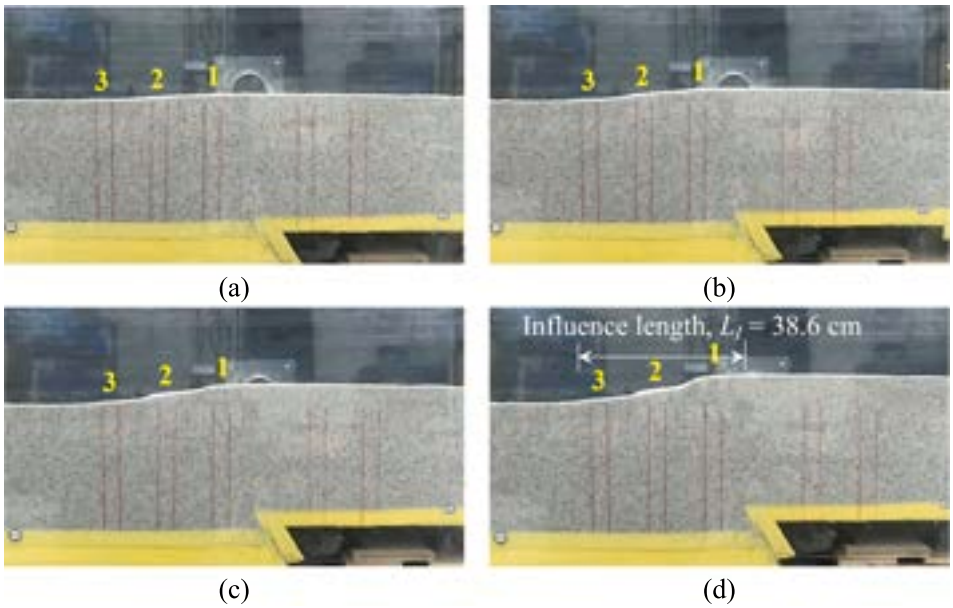

Fig. 16. Photos of baseline GEC foundation test (Test GEC10) at various fault offsets: (a) $S = 1.5$ cm; (b) $S = 3$ cm; (c) $S = 4.5$ cm; and (d) $S = 6$ cm.

cm, which is greater than the fault influence length for the unreinforced foundation ($L_I = 27.7$ cm). Fig. 18 presents the shear strain contours of the GEC foundation subjected to reverse fault movement. As the fault displaced, the fault-induced shear rupture passed through the first and second GEC rows in the footwall (labeled as 1 and 2 in Fig. 18). This mechanism was defined as the shear rupture diffusion effect. The diffusion effect was attributed to the soil–geosynthetic interaction, resulting in the distribution of the fault-induced shear rupture over a wider influence zone (i.e., dissipated the energy of the fault movement). As the fault displacement increased, the fault-induced shear rupture was then partially intercepted by the first GEC row in the footwall. This mechanism was defined as the shear rupture diversion effect. The diversion effect was attributed to the increases in the soil shear strength and stiffness of the GECs, resulting from the increase of the lateral earth pressure acting on the GECs as the fault displaced.

In summary, the baseline GEC foundation considerably reduced the β_{max} at the ground surface for all fault offsets evaluated. The R_d value was 23.3% at $S/H = 30\%$, revealing that the GEC foundation can mitigate the risk of surface fault hazards associated with large reverse fault movement. Two mechanisms, shear rupture diffusion and diversion effects, were identified, depending on the magnitude of the fault displacement and the system stiffness of the GEC foundation.

Comparison of GRS and GEC foundations

Fig. 20a-b present comparisons of the β_{max} and R_d values at various fault offsets for the GRS and GEC foundations, respectively. Test results revealed that both GRS and baseline GEC foundations (labeled as solid squares in Fig. 20a-b) can effectively reduce the β_{max} at the ground surface at small fault offsets. The R_d values of GRS and baseline GEC foundations at $S = 1.5$ cm ($S/H = 7.5\%$) were 30.2% and 33.3%, respectively. However, as the fault offsets increased, the GRS foundation became ineffective (i.e., $R_d = 0\%$ at $S/H = 30\%$) due to insufficient mobilized tensile force within the reinforcement (as discussed in Section 3.2). Meanwhile, the baseline GEC foundation remained effective in reducing β_{max} at large fault offsets, which has the R_d value of 23.3% at S

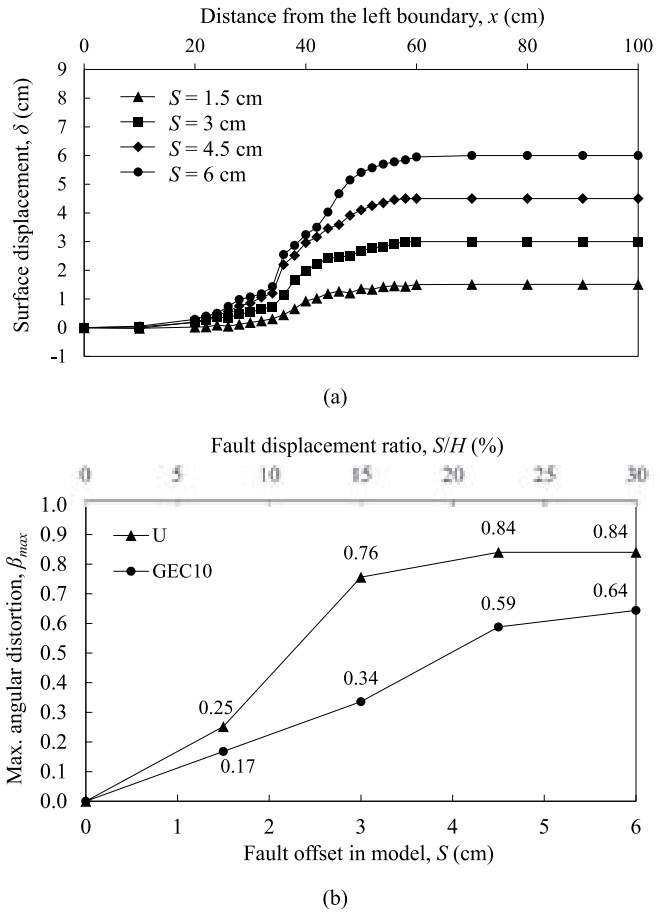

Fig. 17. Ground deformation of baseline GEC foundation test (Test GEC10) at various fault offsets: (a) surface displacement profile; and (b) maximum angular distortion.

= 6 cm (S/H = 30%). As discussed in Section 3.3, the fault-induced shear rupture within the GEC foundation was distributed to a wider influence zone and intercepted by the GECs (i.e., the shear rupture diffusion and diversion effects), resulting in better performance in reducing β_{max} at large fault offsets.

Influence of GEC horizontal spacing

To evaluate the influence of GEC horizontal spacing on the performance of GEC foundations against reverse fault movement, a series of reduced model tests was conducted on GEC foundations with various GEC spacings. The influence of GEC spacing on the effectiveness of GEC foundations in reducing β_{max} at the ground surface and the reinforcing mechanisms associated with shear rupture propagation were investigated. Fig. 19 shows images of the GEC spacing tests at various fault offsets. The center-to-center GEC spacings in Tests GEC8, GEC10, and GEC14 were S_h = 8, 10, and 14 cm, respectively. The minimum GEC horizontal spacing (i.e., S_h = 8 cm) was determined in accordance with the group pile effect, which suggests that the minimum horizontal spacing should be not less than 2.5 times the GEC diameter. The GEC spacing-to-diameter ratio (d_c = 3 cm) in Tests GEC8, GEC10, and GEC14 was S_h/d_c = 2.6, 3.3, and 4.6, respectively. The S_h/d_c ratio was used to identify the optimal GEC spacing for the design of GEC foundations across a reverse fault.

Figs. 20 and 21 present the influence of GEC spacing on the performance of GEC foundations subjected to reverse fault movement. For S_h = 8 cm (S_h/d_c = 2.6), the β_{max} were 0.11, 0.24, 0.63, and 0.71 at S = 1.5, 3, 4.5, and 6 cm, respectively, with the corresponding R_d values of 55.6%, 68.5%, 25%, and 15%, respectively. The GEC foundation with a close GEC spacing considerably reduced the β_{max} at small fault offsets and remained effective in reducing β_{max} even after the shear rupture broke through the ground surface at S = 4.5 cm (S/H = 22.5%). The fault-induced shear rupture was intercepted by the first GEC row due to high system stiffness of the GEC foundation. The major mechanism for the GEC foundation with a close GEC spacing in reducing β_{max} was the shear rupture diversion effect. As the fault offset increased, the fault-induced shear rupture propagated upward along the first GEC row and broke through the ground surface, resulting in high β_{max} at the ground surface.

For S_h = 10 cm (i.e., the baseline case, S_h/d_c = 3.3), as discussed in Section 3.3, the β_{max} at the ground surface was effectively reduced due to the shear rupture diffusion and diversion effects. Additional diffusion of the shear rupture was observed in the GEC foundation with a proper GEC

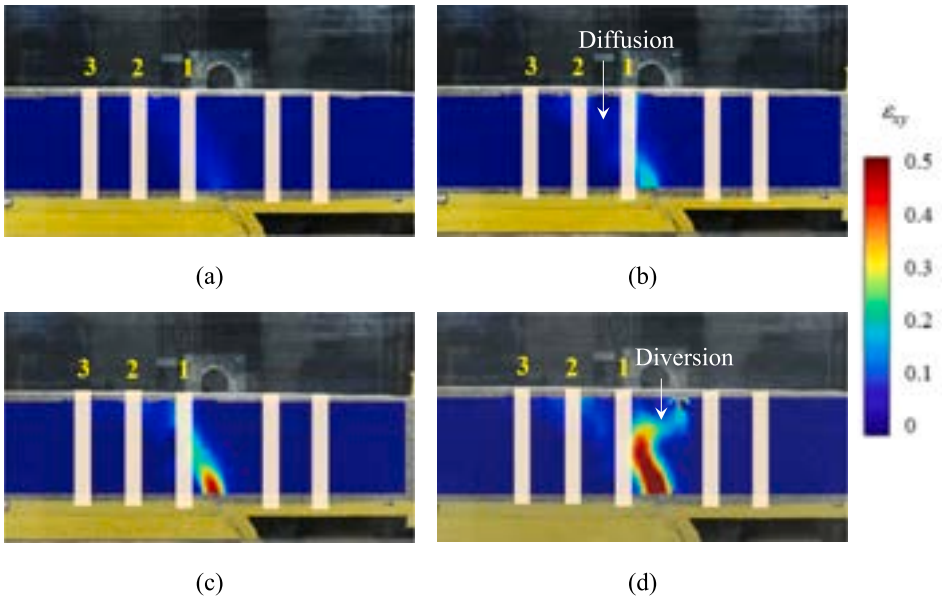

Fig. 18. Shear rupture propagation of baseline GEC foundation test (Test GEC10) at various fault offsets: (a) S = 1.5 cm; (b) S = 3 cm; (c) S = 4.5 cm; and (d) S = 6 cm.

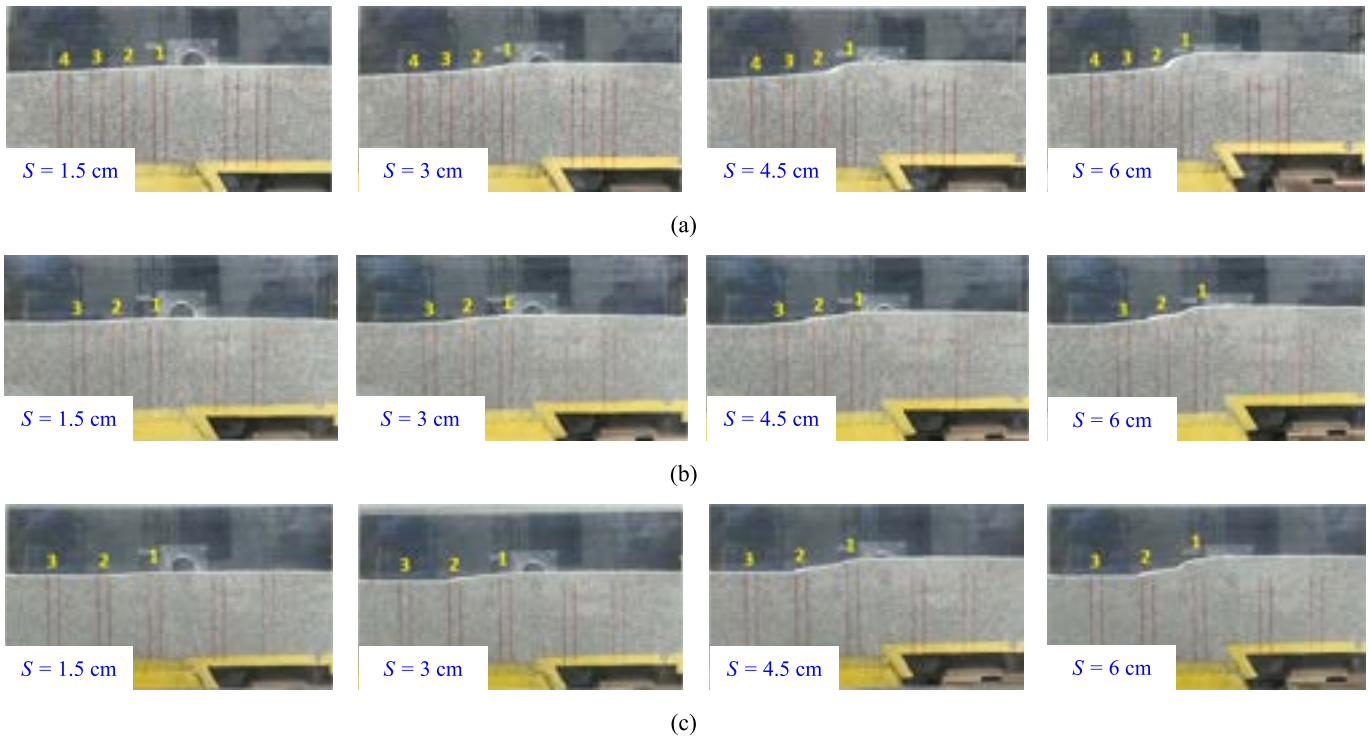

Fig. 19. Photos of GEC spacing tests at various fault offsets: (a) GEC8; (b) GEC10; and (c) GEC14.

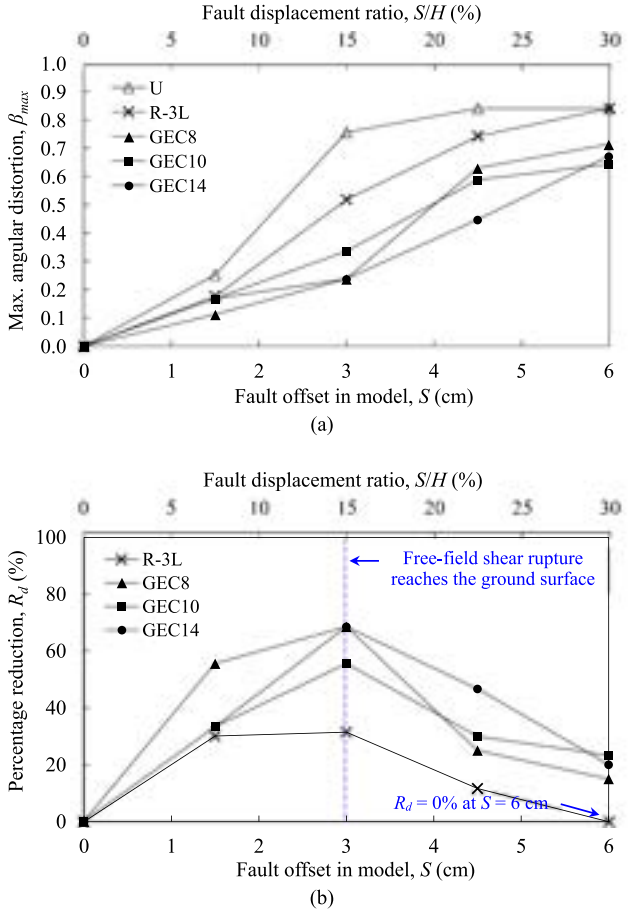

Fig. 20. Influence of GEC horizontal spacing on: (a) β_{max} at ground surface; and (b) percentage reduction R_d.

spacing (i.e., the fault-induced shear rupture passed through the first and second GEC rows in the footwall), resulting in the most significant reduction in β_{max} at large fault offsets. The β_{max} at $S = 6$ cm ($S/H = 30\%$) in Tests GEC8, GEC10, and GEC14 were 0.71, 0.64, and 0.67, respectively, with the corresponding R_d values of 15%, 23.3%, and 20%, respectively.

For $S_h = 14$ cm ($S_h/d_c = 4.6$), the β_{max} were 0.17, 0.24, 0.45, and 0.67 at $S = 1.5$, 3, 4.5, and 6 cm, respectively, with the corresponding R_d values of 33.3%, 68.5%, 46.7%, and 20%, respectively. The β_{max} at the ground surface was effectively reduced by the GEC foundation with a wide GEC spacing. The fault-induced shear rupture only passed through the first GEC row (i.e., the diffusion of shear rupture was limited by the first GEC row) and reached the ground surface between the first and second GEC rows at $S = 3$ cm ($S/H = 15\%$). The diversion of the shear rupture was not observed for wide GEC spacing due to the low system stiffness of the GEC foundation. The shear rupture diffusion effect was the governing mechanism for the GEC foundation with a wide GEC spacing in reducing β_{max}.

In summary, the β_{max} at the ground surface was considerably reduced for all GEC spacings evaluated. Because of complex mechanisms between diversion and diffusion of the shear rupture in the GEC foundations, an optimal GEC spacing of $S_h/d_c = 3.3$ was observed, which exhibited the most significant reduction in β_{max} at large fault offsets.

Design implication

Earthquake magnitudes and maximum displacements can be predicted using the empirical formulations such as that proposed by the U. S. Geological Survey [7], based on the statistical data for 35 cases of historic ground surface faulting in the United States and Mexico. The relationship between the maximum displacement and Richter magnitude of an earthquake is as follows:

$$\text{Log } D = 0.57\, M_L - 3.39 \tag{3}$$

where D is the maximum displacement in feet and M_L is the Richter magnitude. According to the U.S. Geological Survey definition,

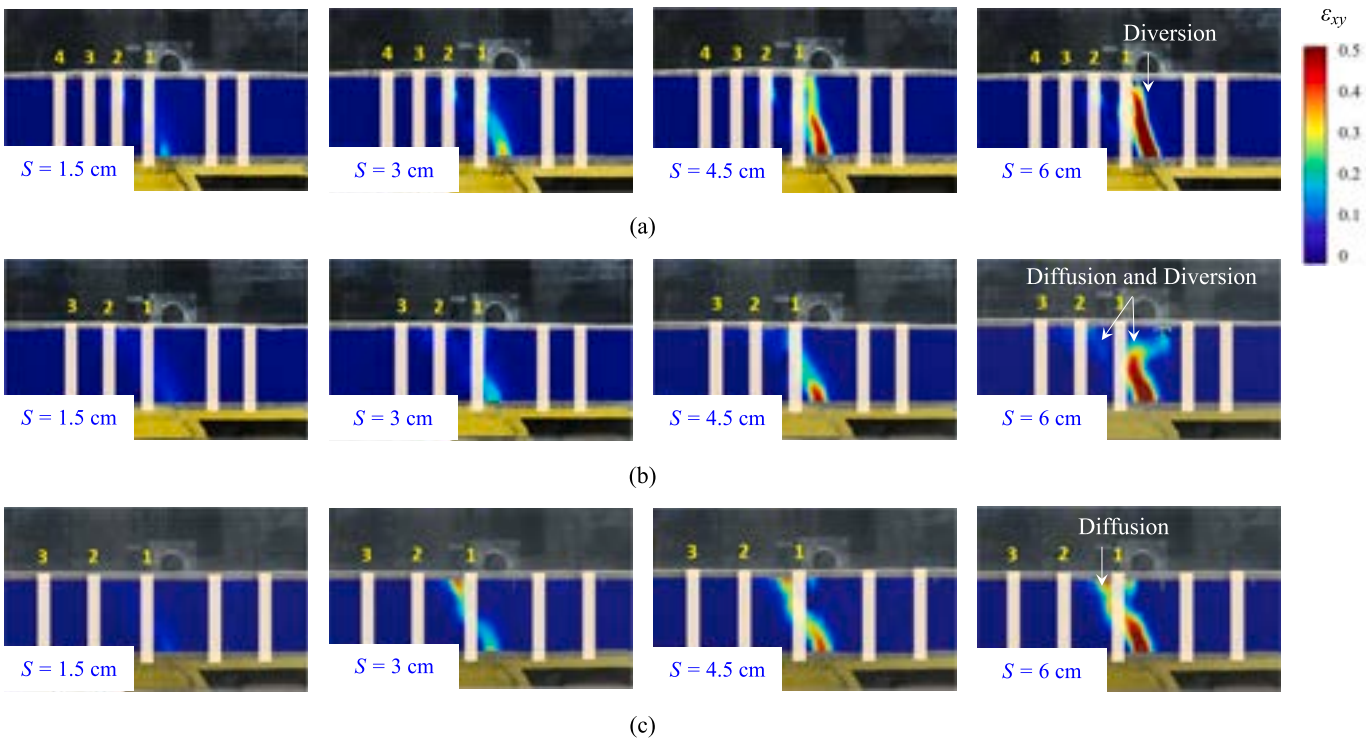

Fig. 21. Influence of GEC horizontal spacing on shear rupture propagation: (a) GEC8; (b) GEC10; and (c) GEC14.

earthquakes are classified as light earthquakes when the Richter magnitude is less than 5.0 ($M_L < 5.0$), moderate earthquakes when $5.0 \leq M_L < 6.0$, and strong earthquakes when $M_L \geq 6.0$. The corresponding maximum displacements for light, moderate, and strong earthquakes calculated using the empirical formula presented in Eq. 3 are $D < 7$ cm, 7 cm $\leq D <$ 32 cm, and $D \geq 32$ cm, respectively. The fault offsets considered in the reduced model tests were $S = 1.5$, 3, 4.5, and 6 cm, which correspond to 0.225, 0.45, 0.675, and 0.9 m, respectively, in prototype (at the target scaling ratio $\lambda = 15$). Therefore, the foundations were subjected to a fault displacement equivalent to a strong earthquake when the fault offset reached $S = 0.45$ m ($S = 3$ cm in the model). Similarly, the foundations were subjected to a fault displacement equivalent to a moderate earthquake for $S = 0.225$ m ($S = 1.5$ cm in the model).

The previous discussion and reduced model test results demonstrate that a GEC foundation can reduce the β_{max} at the ground surface values ranging from 23.3% to 55.6% when a strong earthquake occurs ($M_L \geq$ 6.0), which considerably mitigates the risk of the surface fault hazards associated with reverse fault movements. However, a GRS foundation is only effective in mitigating β_{max} for moderate earthquakes ($M_L =$ 5.0–6.0). Therefore, if embankment construction across a reverse fault rupture zone is unavoidable, GEC foundations are found to be better suited than GRS foundations and can be used as a mitigation measure to reduce the reverse fault-induced ground deformation. It should be noted that the maximum angular distortion at the ground surface might exceed a superstructure's design tolerance despite achieving a considerable reduction in fault-induced ground deformation. For example, the allowable angular distortion for GRS walls with wrap-around facing is $\beta_{allow} = 1/50$ according to FHWA design guidelines [20,32]. However, the main goal of constructing a ductile GEC foundation is to ensure the stability, serviceability and reparability of the overlying embankments or infrastructure when a destructive earthquake fault movement occurs.

Conclusions

In this study, a series of reduced model tests on GEC foundations across a reverse fault was conducted. For comparison, reduced model tests on unreinforced and GRS foundations were also performed. The effectiveness of a GEC foundation to mitigate ground surface deformation induced by reverse fault movement and reinforcing mechanisms of geotextile encasements were investigated. The influence of GEC horizontal spacing on the performance of a GEC foundation was also discussed. Based on the experimental results, the key findings of this study are as follows:

1. For the unreinforced foundation, the fault-induced shear rupture broke through the foundation soil and a distinct rupture occurred at the ground surface at $S/H = 15\%$. Meanwhile, the β_{max} increased considerably, indicating a high surface fault hazard risk. The β_{max} at the ground surface approached the slope of the sand's angle of repose at large fault offsets.
2. For the GRS foundation, the β_{max} at the ground surface was notably reduced at small fault offsets. However, the GRS foundation became ineffective in reducing β_{max} at large fault offsets. The R_d value decreased to 0% at $S/H = 30\%$ due to insufficient mobilized tensile force within the reinforcement because the GRS foundation was mainly subjected to compression as reverse fault displaced.
3. For the baseline GEC foundation, the β_{max} at the ground surface for all fault offsets evaluated was considerably reduced. The GEC foundation was effective in reducing β_{max} at large fault offsets. The R_d value was 23.3% at $S/H = 30\%$, revealing that the GEC foundation can mitigate the risk of surface fault hazards associated with large reverse fault movement.
4. Two mechanisms, shear rupture diffusion and diversion effects, were identified, depending on the magnitude of the fault displacement and the system stiffness of the GEC foundation. The diffusion effect was attributed to the soil–geosynthetic interaction, resulting in the distribution of the fault-induced shear rupture over a wider influence zone. The diversion effect was attributed to the increases in the soil shear strength and stiffness of GECs, resulting from the increase of the lateral earth pressure acting on the GECs as the fault displaced.

5. For all GEC spacings evaluated, the β_{max} at the ground surface was considerably reduced. Because of complex mechanisms between diversion and diffusion of the shear rupture in the GEC foundations, an optimal GEC spacing of $S_h/d_c = 3.3$ was observed, which exhibited the most significant reduction in β_{max}.
6. Based on the classification of earthquakes and the corresponding maximum displacements converted, GEC foundations have superior performance than GRS foundations in mitigating fault-induced ground deformation as a strong earthquake occurred ($M_L \geq 6.0$, $S \geq 0.32$ m in prototype).

CRediT authorship contribution statement

Jung Chiang: Conceptualization, Methodology, Investigation, Writing – original draft, Writing – review & editing. **Emerson Edwige Michel:** Methodology, Investigation, Writing – review & editing. **Kuo-Hsin Yang:** Conceptualization, Writing – review & editing, Supervision. **Jorge G. Zornberg:** Writing – review & editing, Supervision.

Declaration of Competing Interest

The authors declare that they have no known competing financial interests or personal relationships that could have appeared to influence the work reported in this paper.

Data availability

No data was used for the research described in the article.

Acknowledgment

The concepts researched herein were motivated by an actual project involving a GRS structure across an active fault designed by Sinotech Engineering Consultants. The authors sincerely appreciate Sinotech's support for providing design information. The first author would like to acknowledge the Ph.D. Student Research Abroad Program funded by Ministry of Science and Technology, Taiwan for his study at the University of Texas at Austin. This research was supported by the Ministry of Science and Technology, Taiwan under grant number MOST111-2628-E-002-003-MY2.

References

[1] Almeida MS, Hosseinpour I, Riccio M, Alexiew D. Behavior of geotextile encased granular columns supporting test embankment on soft deposit. J Geotech Geoenviron Eng 2015;141(3):04014116.
[2] Ashtiani M, Ghalandarzadeh A, Mahdavi M, Hedayati M. Centrifuge modeling of Geotechnical mitigation measures for shallow foundations subjected to reverse faulting. Can Geotech J 2017;55(8):1130–43.
[3] ASTM D4595. Standard Test Method for Tensile Properties of Geotextiles by the Wide-Width Strip Method. West Conshohocken, US: ASTM International; 2009.
[4] ASTM D5321. Standard Test Method for Determining the Shear Strength of Soil-Geosynthetic and Geosynthetic-Geosynthetic Interfaces by Direct Shear. West Conshohocken, US: ASTM International; 1997.
[5] ASTM D7181. Standard Test Method for Consolidated Drained Triaxial Compression Test for Soils. West Conshohocken, US: ASTM International 2011.
[6] Basack S, Indraratna B, Rujikiatkamjorn C. Modeling the performance of stone column-reinforced soft ground under static and cyclic loads. J Geotech Geoenviron Eng 2016;142(2):04015067.
[7] Bonilla MG. Historic surface faulting in the continental United States and adjacent parts of Mexico. US Geological Survey 1967:TID-24124.
[8] Bray JD, Ashmawy A, Mukhopadhyay G, Gath EM. Use of geosynthetics to mitigate earthquake fault rupture propagation through compacted fill. In:Proceedings of the Geosynthetics'93 Conference, Vancouver, Canada, 1993; 1:379–392.
[9] Bray JD, Seed RB, Cluff LS, Seed HB. Earthquake fault rupture propagation through soil. J Geotech Eng (ASCE) 1994;120(3):543–61.
[10] Bray JD. Developing mitigation measures for the hazards associated with earthquake surface fault rupture. A Workshop on Seismic Fault-Induced Failures-Possible Remedies for Damage to Urban Facilities. Japan: Japan Society for Promotion of Science, University of Tokyo; 2001.
[11] Bray JD. Earthquake surface fault rupture design considerations. In: Proceedings of the Sixth International Conference on Urban Earthquake Eng, Tokyo, Japan, 2009; 37–45.
[12] Buckingham E. On physically similar systems; illustrations of the use of dimensional equations. Phys Rev 1914;4(4):345–76.
[13] Cengiz C, Kilic IE, Guler E. On the shear failure mode of granular column embedded unit cells subjected to static and cyclic shear loads. Geotext Geomembr 2019;47(2):193–202.
[14] Chen JF, Li LY, Xue JF, Feng SZ. Failure mechanism of geosynthetic encased stone columns in soft soils under embankment. Geotext Geomembr 2015;43:424–31.
[15] Chen JF, Wang XT, Xue JF, Zeng Y, Feng SZ. Uniaxial compression behavior of geotextile encased stone columns. Geotext Geomembr 2018;46(3):277–83.
[16] Chen YG, Chen WS, Lee JC, Lee YH, Lee CT. Surface rupture of 1999 Chi-Chi earthquake yields insights on active tectonics of central Taiwan. Bull Seismol Soc Am 2001;91(5):977–85.
[17] Chiang J, Yang KH, Chan YH, Yuan CL. Finite element analysis and design method of geosynthetic-reinforced soil foundation subjected to normal fault movement. Comput Geotech 2021;139:104412.
[18] Das SK, Bora MC. Improved performance of soft clay foundations using stone columns and geocell-sand mattress. Geotext Geomembr 2013;41:26–35.
[19] Dash SK, Bora MC. Influence of geosynthetic encasement on the performance of stone columns floating in soft clay. Can Geotech J 2013;50(7):754–65.
[20] Elias V, Christopher BR, Berg R. Mechanically Stabilized Earth Walls and Reinforced Soil Slopes Design and Construction Guidelines. FHWA-NHI-00-043, Washington, D.C. 2001.
[21] Faccioli E, Anastasopoulos I, Gazetas G, Callerio A, Paolucci R. Fault rupture–foundation interaction: selected case histories. Bull Earthq Eng 2008;6(4):557–83.
[22] Fadaee M, Ezzatyazdi P, Anastasopoulos I, Gazetas G. Mitigation of reverse faulting deformation using a soil bentonite wall: dimensional analysis, parametric study, design implications. Soil Dyn Earthq Eng 2016;89:248–61.
[23] Firouzeh FH, Payan M, Chenari RJ, Shafiee A, Senetakis K. Efficiency of various mitigation schemes in the alleviation of the destructive effect of reverse dip-slip fault rupture on surface and embedded shallow foundations using upper bound finite element limit analysis. Comput Geotech 2022;142:104548.
[24] Garcia EF, Gallage CPK, Uchimura T. Function of permeable geosynthetics in unsaturated embankments subjected to rainfall infiltration. Geosynth Int 2007;14(2):89–99.
[25] Garcia FE, Bray JD. Discrete element analysis of earthquake fault rupture-soil-foundation interaction. J Geotech Geoenviron Eng (ASCE) 2019;145(9):04019046.
[26] Garcia FE, Bray JD. Discrete-element analysis of influence of granular soil density on earthquake surface fault rupture interaction with rigid foundations. J Geotech Geoenviron Eng (ASCE) 2019;145(11):04019093.
[27] Gazetas G, Pecker A, Faccioli E, Paolucci R, Anastasopoulos I. Preliminary design recommendations for dip-slip fault–foundation interaction. Bull Earthq Eng 2008;6(4):677–87.
[28] Gniel J, Bouazza A. Improvement of soft soils using geogrid encased stone columns. Geotext Geomembr 2009;27(3):167–75.
[29] Gu M, Han J, Zhao M. Three-Dimensional discrete-element method analysis of stresses and deformations of a single geogrid-encased stone column. Int J Geomech 2017;17(9):04017070.
[30] Gu M, Zhao M, Zhang L, Han J. Effects of geogrid encasement on lateral and vertical deformations of stone columns in model tests. Geosynth Int 2016;23(2):100–12.
[31] Hasan M, Samadhiya NK. Performance of geosynthetic-reinforced granular piles in soft clays: model tests and numerical analysis. Comput Geotech 2017;87:178–87.
[32] Holtz RD, Cristopher BR, Berg RR. Geosynthetic design and construction guidelines. FHWA HI-95-038, McLean, Virginia; 1998.
[33] Hong YS, Wu CS, Yu YS. Model tests on geotextile-encased granular columns under 1-g and undrained conditions. Geotext Geomembr 2016;44(1):13–27.
[34] Hosseinpour I, Almeida MSS, Riccio M. Full-scale load test and finite-element analysis of soft ground improved by geotextile-encased granular columns. Geosynth Int 2015;22(6):428–38.
[35] Lin ML, Chung CF, Jeng FS. Deformation of overlying soil induced by thrust fault slip. Eng Geol 2006;88:70–89.
[36] Loli M, Kourkoulis R, Gazetas G. Physical and numerical modeling of hybrid foundations to mitigate seismic fault rupture effects. J Geotech Geoenviron Eng (ASCE) 2018;144(11):04018083.
[37] Mohapatra SR, Rajagopal K, Sharma J. Direct shear tests on geosynthetic-encased granular columns. Geotext Geomembr 2016;44(3):396–405.
[38] Murugesan S, Rajagopal K. Shear load tests on stone columns with and without geosynthetic encasement. Geotech Test J 2008;32(1):35–44.
[39] Oettle NK, Bray JD. Geotech mitigation strategies for earthquake surface fault rupture. J Geotech Geoenviron Eng (ASCE) 2013;139(11):1864–73.
[40] Rathod D, Abid MS, Vanapalli SK. Performance of polypropylene textile encased stone columns. Geotext Geomembr 2021;49(1):222–42.
[41] Viswanadham BVS, König D. Studies on scaling and instrumentation of a geogrid. Geotext Geomembr 2004;22(5):307–28.
[42] Yang KH, Chiang J, Lai CW, Han J, Lin ML. Performance of geosynthetic-reinforced soil foundation across a normal fault. Geotext Geomembr 2020;48(3):357–73.
[43] Yasuhara K, Recio-Molina J. Geosynthetic-wrap around revetments for shore protection. Geotext Geomembr 2007;25(4–5):221–32.
[44] Yoo C, Tabish JW, Yang Q, Abbas JS, Song S. Effect of internal drainage on deformation behavior of GRS wall during rainfall. Geosynth Int 2022;29(2):137–50.
[45] Zhang L, Peng B, Xu Z, Zhou S. Shear performance of geosynthetic-encased stone column based on 3D-DEM simulation. Comput Geotech 2022;151:104952.